Transport barrier in 5D gyrokinetic flux-driven simulations

G. Lo-Cascio, Etienne Gravier, T. Réveillé, M. Lesur, Y. Sarazin, X. Garbet, L. Vermare, K. Lim, A. Guillevic, V. Grandgirard

Transport barrier in 5D gyrokinetic flux-driven simulations

G. Lo-Cascio[1], E. Gravier[1], T. Réveillé[1], M. Lesur[1], Y. Sarazin[2], X. Garbet[2], L. Vermare[3], K. Lim[4], A. Guillevic[1], and V. Grandgirard[2]

[1]Université de Lorraine, CNRS, IJL, F-54000 Nancy, France
[2]CEA, IRFM, F-13108 Saint-Paul-lez-Durance, France
[3]Ecole Polytechnique, LPP, CNRS UMR 7648, 91128 Palaiseau, France
[4]Swiss Plasma Center, CH-1015 Lausanne, Switzerland

August 31, 2022

Abstract

Two ways for producing a transport barrier through strong shear of the $\mathbf{E}\times\mathbf{B}$ poloidal flow have been investigated using GYSELA gyrokinetic simulations in a flux-driven regime. The first one uses an external poloidal momentum (i.e. vorticity) source that locally polarizes the plasma, and the second one enforces a locally steep density profile that also stabilizes the Ion Temperature Gradient (ITG) instability modes linearly. Both cases show a very low local turbulent heat diffusivity coefficient χ_T^{turb} and a slight increase in core pressure when a threshold of $\omega_{E\times B} \approx \overline{\gamma}_{lin}$ (respectively the $E \times B$ shear rate and average linear growth rate of ITG) is reached, validating previous numerical results. This pressure increase and χ_T^{turb} quench are the signs of a transport barrier formation. This behaviour is the result of a reduced turbulence intensity which strongly correlates with the shearing of turbulent structures as evidenced by a reduction of the auto-correlation length of potential fluctuations as well as an intensity reduction of the k_θ spectrum. Moreover, a small shift towards smaller poloidal wavenumber is observed in the vorticity source region which could be linked to a tilt of the turbulent structures in the poloidal direction.

1 Introduction

Transport is an important topic in magnetic confinement fusion devices because of its impact on the reactor efficiency. On top of neoclassical transport [1] (i.e. outward radial transport), the dominant loss channel is the turbulent one [2][3][4]. This transport is mainly due to micro-instabilities [5][6] leading to large values of heat conductivity and radial heat fluxes. Ion Temperature Gradient (ITG) [7][8], Trapped Electron Modes (TEM) [9][10], Parallel Velocity Gradient (PVG) [11] and transverse Kelvin-Helmholtz modes [12] are exemples of such instabilities.

However, overall transport can be reduced (i.e. increasing confinement time) by triggering a plasma transition to an improved confinement state. Such a transition involves

the creation of a transport barrier which can be localized in the plasma core (ITB for Internal Transport Barrier) or at the edge (ETB for Edge Transport Barrier, H-mode [13][14][15]). Many tokamaks are able to trigger ITBs (e.g. EAST [16], KSTAR [17], JET [18], DIII-D [19] and JT-60U [20]) or ETBs (e.g. DIII-D [21][22], JFT-2M [23], Alcator C-mod [24], JET [25], ASDEX [13] and ASDEX Upgrade [26][27], COMPASS [28] and MAST [29]) when a certain power threshold is exceeded. Recently, HL-2A experiments [30] showed both kind of transport barriers (i.e. DTB for Dual Transport Barrier) happening simultaneously during high-β_p scenarios. While ITBs and ETBs happen in distinct environments, they share many important properties such as a radially localized steep pressure gradient and a strong radial electric field. As a result a strong poloidal $E \times B$ shear flow is generated. Part of this shearing (i.e. zonal flows [31][32][33]) is generated by turbulence and leads to a self-regulated state through a prey-predator mechanism [34].

The effects of shear flow on a turbulent plasma have been studied [35][36][37] using different theoretical explanations for the underlying mechanisms leading to a transport quench. The main hypothesis which will be explored here is that large scale turbulent structures are suppressed and teared by $E \times B$ poloidal shearing. The radial correlation length and correlation time are greatly reduced by shear flow that reduces the transport as a result. Another hypothesis proposes a turbulence intensity reduction due to this same shear flow. An empiric criterion gives an estimate of the needed $\omega_{E\times B}$, the $E \times B$ shear rate, which should be within the same order as γ_{lin}^{max}, the maximum linear growth rate of the instability [5], to suppress turbulence.

We propose here to extend a previous study of A. Strugarek [38][39] using an updated version of GYSELA, a full-f 5D gyrokinetic code, using a vorticity source to produce a sheared poloidal momentum profile. In section 2, we give a brief description of the model used in GYSELA and the construction of the vorticity source term used. Simulation conditions and parameters are given in section 3. Section 4 is dedicated to the onset of a transport barrier using the vorticity source. A slight increase of pressure in the core region as well as a diffusivity reduction in the source region are observed. Turbulent structures are torn appart by the shear flow as attested by the reduction in auto correlation length. A reduction in turbulence intensity is also observed once the shear rate exceeds a certain threshold. Section 5 focuses on a transport barrier triggered by a fixed steep density gradient profile which stabilizes linearly the ITG modes at the steep gradient position. The correlation length and turbulent diffusivity are also greatly reduced at the steep gradient location. A conclusion is provided in section 6.

2 Model and source term

GYSELA [40] is a 5D full-f gyrokinetic [41] electrostatic code coupling the Vlasov equation and the quasi-electroneutrality equation. The electron density response is taken adiabatic so that, up to compressional effects, the time-averaged particle transport across circular magnetic surfaces vanishes. The following set of equations are solved for deuterium ions:

$$B_{\parallel}^{\star}\partial_t \bar{F} + \nabla \cdot \left(\dot{\mathbf{x}}_{GC} B_{\parallel}^{\star} \bar{F}\right) + \partial_{v_{G\parallel}} \left(\dot{v}_{G\parallel} B_{\parallel}^{\star} \bar{F}\right) = \mathcal{C}\left(\bar{F}\right) + \mathcal{S}, \tag{1}$$

$$en_{e_0}\left(\frac{\phi - \langle\phi\rangle_{FS}}{T_e}\right) - Z_i \nabla_{\perp} \cdot \left(\frac{n_0}{B_0 \omega_{c,i}} \nabla_{\perp}\phi\right) = Z_i \int dv \mathcal{J}\left[\bar{F} - \bar{F}_{eq}\right], \tag{2}$$

$$B_{\parallel}^{\star}\dot{\mathbf{x}}_{GC} = v_{G\parallel}\mathbf{B}^{\star} + \frac{1}{Z_i}\mathbf{b} \times \nabla\Lambda, \tag{3}$$

$$B_{\parallel}^{\star} m_i \dot{v}_{G\parallel} = -\mathbf{B}^{\star} \cdot \nabla\Lambda. \tag{4}$$

Here, $\bar{F}$ is the ion gyrocentre distribution function, ϕ the electrostatic potential, $\mathbf{x}_{GC}$ and $v_{G\parallel}$ the gyro-center position and parallel velocity, Z_i and m_i the charge number and particle mass of the main ion species (deuterium here), B_0 the magnetic field amplitude and $\omega_{c,i} = Z_i e B_0/m_i$ the ion cyclotron pulsation. Here, dv is defined by $dv = J_v d\mu dv_{\parallel}$ with $J_v = 2\pi B_{\parallel}^{\star}/m_i$, the velocity space Jacobian, which is defined through $\mathbf{b} = \mathbf{B}/\left\|\mathbf{B}\right\|$ and $B_{\parallel}^{\star} = \mathbf{B}^{\star} \cdot \mathbf{b} = B + \frac{m_i}{q_i} v_{G\parallel} \mathbf{b} \cdot (\nabla \times \mathbf{b})$, with

$$\mathbf{B}^{\star} = \mathbf{B} + \frac{m_i}{q_i} v_{G\parallel} \nabla \times \mathbf{b}. \tag{5}$$

$\mathcal{J}$ is the gyro-average operator, $\mathcal{C}\left(\bar{F}\right)$ is the collision operator which conserves energy and particles [42], and $\Lambda = eZ_i\mathcal{J}\left[\phi\right] + \mu B$ is the gyrocenter energy with $\mu = m_i v_{\perp}^2/2B$ the magnetic moment. $\mathcal{S}$ represents the source terms, including for example the heat source and/or the poloidal momentum (equivalent to a vorticity) source. The average over a flux-surface is defined by $\langle \ldots \rangle_{FS} = \iint \ldots J_{\chi} d\theta d\varphi / \iint J_{\chi} d\theta d\varphi$ with $J_{\chi} = (\mathbf{B} \cdot \nabla\theta)^{-1}$ the flux-surface jacobian. The kinetic source of poloidal momentum, also referred as a vorticity source term, is defined as

$$\mathcal{S}_{\Omega} = \frac{m v_{G\parallel}^2 - \mu B}{T_s} S_r\left(r\right) S_0^{\Omega} \exp\left(-\frac{\frac{1}{2} m v_{G\parallel}^2 + \mu B}{T_s}\right) \tag{6}$$

with S_0^{Ω} the source amplitude, $S_r\left(r\right)$ the radial profile and T_s the source temperature. The former two are GYSELA input parameters while the latter is fixed at $T_s/T_0 = 1$ where T_0 a reference temperature. This source is built such that no heat nor particles are injected in the system. A marginal quantity of parallel momentum is injected along with the poloidal momentum as well as a pressure anisotropy which will be discussed in section 3. The mathematical construction of the heat and vorticity sources are detailed in [43] and [44].

The vorticity conservation equation is given by

$$\partial_t W + \partial_r \mathcal{K} = S_0 \nabla_{\perp}^2 S_r \tag{7}$$

with $W = -\left\langle \nabla \cdot \left(\frac{n_{eq,s} m_s}{B^2} \nabla_{\perp}\phi\right)\right\rangle_{FS} = e\left\langle \int dv \mathcal{J}\left[\bar{F}\right]\right\rangle_{FS}$ the fluid vorticity , $\mathcal{K} = e\left\langle \int dv^{\star} \mathcal{J}\left[\left(d_t \mathbf{x}_G \cdot \nabla r\right) \bar{F}\right]\right\rangle_{FS}$ the fluid vorticity flux and $S_0 \nabla_{\perp}^2 S_r$ the fluid vorticity source. Figure 1 (orange dashed line) represents the normalized fluid vorticity source profile as a function of the normalized radius. One can note the main central lobe at $r/a = 0.75$ which is later referred as the source location. This equation (7) is obtained by taking the gyro average of the Vlasov equation (1) and integrating over the velocity space.

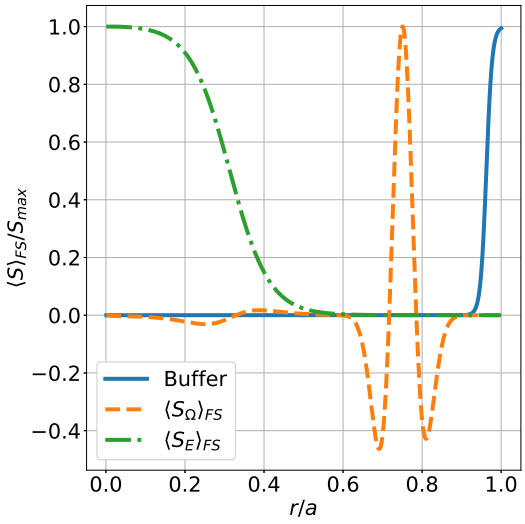

Figure 1: Normalized radial profiles of the buffer diffusion (blue line), fluid energy source (dotted green line) and fluid vorticity source (dashed orange line).

A flux-surface average is then performed to obtain a 1D (i.e. radial) equation for vorticity.

It is difficult to impose a sheared radial electric field E_r in a full-f code; trying to inject such a field directly in the quasi-neutrality equation proved to be uneffective [45] due to immediate screening effect of the plasma. Two different approaches can then be considered to generate an $E \times B$ flow shear in a flux-driven gyrokinetic simulation with adiabatic electrons:

1. Use the poloidal momentum source (also referred to as vorticity source hereafter) previously described. The idea is to add a term in the right-hand-side of the Vlasov equation (1) to polarize the plasma. It adds a small term equivalent to a polarization density, effectively biasing locally the plasma and creating a local E_r field. Ion cyclotron frequency range can be used to inject poloidal momentum in a plasma [46], like IBW (Ion Berstein Waves) [47] or MCFD (Mode Conversion Flow Drive) [48] for example. The poloidal momentum source used in this study can be viewed as the resulting effect of such experimental methods on the sole mean radial electric field. This source aims at emulating the effects of such heating systems and demonstrating the effect of a strong $E \times B$ shear flow on a turbulent plasma.

2. Locally enforce a sheared radial electric field via the radial force balance by "imposing" a large pressure gradient:

$$E_r = -\frac{1}{e_i n_i}\frac{\partial P_\perp}{\partial r} + v_\theta B_\varphi - v_\varphi B_\theta \tag{8}$$

   Notice that, when the pressure is anisotropic, the perpendicular pressure $P_\perp$[1] enters the radial force balance instead of the total pressure P_{tot}. Details on its derivation

[1]More precisely, there should be an additional term to $\partial_r P_\perp$, namely $(P_\parallel - P_\perp)\boldsymbol{\kappa}$, with $\boldsymbol{\kappa} = [\boldsymbol{\nabla}_\perp B - \mathbf{b}\times(\boldsymbol{\nabla}\times\mathbf{B})]/\mathbf{B}$ the magnetic curvature (see for instance [49], eq.6.42]). This contribution is usually small and has been neglected here.

are given in appendix E of [43]. Since radial particle transport is negligible with adiabatic electrons, we expect the imposed density gradient to remain unchanged and a sheared E_r to be generated to balance out the pressure gradient throughout the simulation. This case is referred as the steep gradient case hereafter. We expect the steep density gradient to be the dominant stabilizing mechanism of turbulence since density gradient is long known to stabilize the ITG instabilities [7].

3 Parameters and saturation level

3.1 Simulation parameters

Three simulations with similar parameters are studied; the vorticity and reference cases are two branches of the same initial simulation where in the former the source is activated from $t\omega_{c,0} = 126400$ while the source remains off in the latter. The third one is the so-called steep-gradient case. All of them use a normalized gyro radius $\rho^\star = \rho_0/a \equiv 1/200$ with ρ_0 the hydrogen Larmor radius at mid-radius and a the minor radius. Due to the increasing cost of simulations with smaller $\rho^\star$ values, we chose one comparable to the COMPASS tokamak. The domain goes from $r/a = 0$ to $r/a = 1$ with the last 10% of the radial domain subject to a buffer diffusion region to damp out fluctuations at the edge and avoid possible numerical oscillations. Dirichlet boundary conditions are used at the outer radial position $r/a = 1$ such that $\phi\left(r/a = 1\right) = 0$. There, a buffer region located at $r/a > 0.9$ and characterized by additional diffusion and Krook terms forces the distribution function to relax towards an axisymmetric centered Maxwellian. There is no inner boundary condition since the simulated domain encompasses the magnetic axis $r/a = 0$. Note however that, because of symmetry reasons, the axisymmetric $(m, n) = (0, 0)$ component of the radial electric field is necessarily vanishing at $r/a = 0$. The buffer radial profile is shown on figure 1 (solid blue line). The safety factor radial profile writes

$$q\left(r\right) = 1.5 + 2.3\exp\left[2.5\ln\left(r/a\right)\right]. \tag{9}$$

The resulting magnetic shear $s = \frac{r}{q}\frac{dq}{dr}$ stabilizes the transverse Kelvin-Helmholtz instability that could be driven by the imposed strong $E \times B$ shear [50][51]. However we do not expect the magnetic shear to play a major role in creating the transport barrier since it is monotonic unlike in ITBs scenarios. The isotropic heat source used in those simulations, localized in the interval $r/a = 0$ to $r/a \approx 0.4$ (See figure 1, dotted green line), evolves in time: for the vorticity and reference cases, the amplitude of the heat source is fixed at a "high" value until turbulence intensity saturates. The heat source amplitude is then lowered so that the pressure profile stays roughly constant (i.e., its evolution becomes very slow in time). For the steep gradient case, the source amplitude is fixed at the same "high" value throughout the whole duration of the simulation. The Deuterieum ions are in the banana regime with a collisionality such that $\nu^\star_{D^+} < 1$. Parameters are summarized in table 1.

3.2 Initial conditions

The initial temperature and density profiles are chosen such that ITG instabilities arise, meaning the ratio $\eta \equiv \frac{T^{-1}\partial_r T}{n^{-1}\partial_r n} = \kappa_T/\kappa_n = 3$ is constant on most of the domain except in

the steep gradient case that peaks at $\kappa_n \approx 28$ at $r/a = 0.75$ (see section 5) leading to $\eta \approx 0.13$ locally. The vorticity and reference cases density profile (figure 2a, dashed blue line) is close to a L-mode profile whereas the steep gradient one (figure 2a, dotted orange line) is similar (i.e. in general shape and not in radial position) to what can be observed in H-mode discharges with a steep density gradient at the edge (See [28] for example). Their respective η profiles are shown on figure 2b; the vorticity and reference cases are identical to the steep gradient case except at $r/a = 0.75$, where the steep gradient is located.

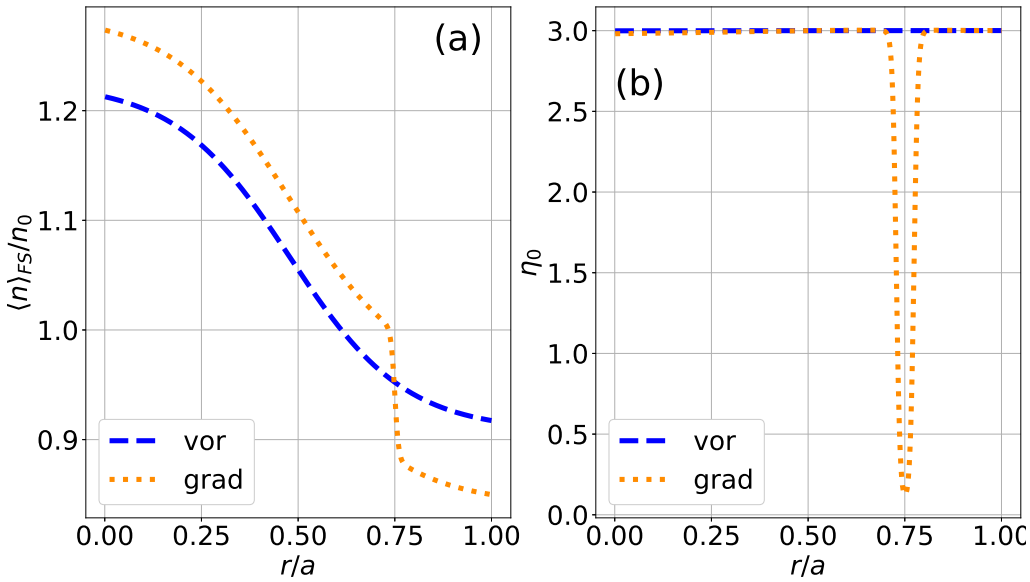

Figure 2: Radial profiles of the flux surface averaged guiding-center density **(a)** and eta profile $\kappa_{T_0}/\kappa_{n_0}$ **(b)** at $t\omega_{c,0} = 0$ for the vorticity case (similar to the reference case, blue dotted line) and for the steep gradient case (orange dashed line).

3.3 Saturation level

We denote each mode as (m, n), where m and n are the poloidal and toroidal Fourier mode numbers respectively. Figure 3 shows the time evolution of the $(0, 0)$ and $(0, 1)$ as well as some resonant $n + m/q\,(r) = 0$ modes of the electrostatic potential, with $q\,(r)$ the safety factor profile, at $r/a = 0.5$ in the reference simulation. All three simulations exhibit very similar behaviours until saturation since the parameters are almost identical (except near the density gradient at $r/a = 0.75$). The oscillating phase of the $(0, 0)$ and $(0, 1)$ modes from $t\omega_{c,0} = 0$ to $t\omega_{c,0} \approx 3 \cdot 10^4$ corresponds to the relaxation of the low frequency GAMs [52] (Geodesic Acoustic Modes). These oscillations are negligeable after the main plasma instability starts its linear growth, namely ITG. This linear growth phase starts at around $t\omega_{c,0} \approx 3 \cdot 10^4$ until turbulence saturation is reached at approximately $t\omega_{c,0} \approx 6 \cdot 10^4$. For each simulation, the global mean linear growth rate $\overline{\gamma}_{lin} \approx 5 \cdot 10^{-4}\omega_{c,0}$ is computed by fitting the linear part on

$$\langle \phi \rangle_{RMS} = \sqrt{\sum_{m,n \neq 0} |\phi_{m,n}|^2}. \tag{10}$$

Values for the different simulations are reported on table 1.

Parameters	Reference	Vorticity	Steep gradient
Collision rate	$\nu^{\star}_{D+}\,(r/a=0.5)=0.1$		
Charge / atomic numbers	$Z_i=1, A_i=2$		
Time step	$\Delta t\omega_{c,0}=16$		
$N_r\times N_\theta\times N_\varphi\times N_{v_\parallel}\times N_\mu$	$511\times 512\times 64\times 127\times 31$		
Normalized gyroradius	$\rho^{\star}=\rho_{c,0}/a=1/200$		
Inverse aspect ratio	$1/\epsilon=R_0/a=4.4$		
Maximum density gradient	$\kappa_n=R_0/L_n=2.2$		$\kappa_n\approx 28$
Maximum temperature gradient	$\kappa_T=R/L_T=6.6$		
Amplitude of vorticity source	$S_0^{\Omega}=0$*	$S_0^{\Omega}=0.08$*	$S_0^{\Omega}=0$
Average ITG linear growth rate	$\overline{\gamma_{lin}}/\omega_{c,0}\approx 5\cdot 10^{-4}$		

Table 1: Simulation parameters used in this study. *The poloidal momentum source is activated from $t\omega_{c,0}=126400$ for the vorticity case and disabled in the reference case.

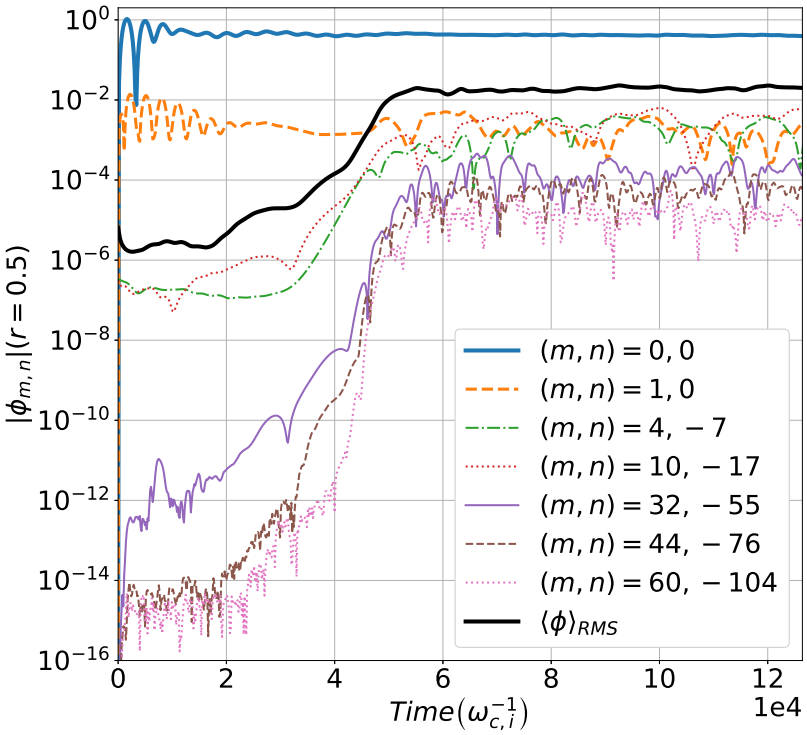

Figure 3: $|\phi_{m,n}|$ at $r=0.5$ plotted against time (up to $t_{vor}\omega_{c,0}=126400$, the vorticity activation time). The solid black line represents $\langle\phi\rangle_{RMS}$ (equation 10) and is used to compute the average linear growth rate of ITG instability. This plot is also representative of the steep gradient case since we look at the mode evolution at $r/a=0.5$, away from the steep gradient region at $r/a=0.75$.

4 Poloidal momentum (vorticity) source

4.1 Onset of a transport barrier

The source described in equation (6) is used to produce a sheared poloidal momentum profile to the system once turbulence intensity saturates. Although already using about 4 million CPU hours, the simulation has not reached steady state yet, which would have required several confinement times. However, the adiabatic evolution of the flux-surface averaged profiles and the fast response of turbulence is enough to reach critical conclusions regarding the impact of an external source of ExB shearing on turbulent transport. Figure 4a shows the $E \times B$ poloidal flow at the same simulation time for both the reference (green dotted line) and vorticity (blue dashed line) cases. The vorticity source effectively produces the desired $E \times B$ flow shear compared to the reference case with a significant amplitude difference at $r/a = 0.7$ and $r/a = 0.8$. As stated in [53], it is empirically found in numerical simulations that the $\omega_{E\times B}$ shearing rate should be within the same order of magnitude as γ_{lin}^{MAX}, the maximum linear growth rate of the relevant instability (i.e. ITG in this case) for turbulence stabilization. This simple rule of thumb is useful to have an idea of the amount of shear we should impose on the plasma *a priori*. Here we choose to normalize the shearing rate to $\overline{\gamma}_{lin} \leqslant \gamma_{lin}^{MAX}$ the average linear growth rate computed with $\langle\phi\rangle_{RMS}$ (equation 10) which is more representative of the actual "growth rate of ITG" instability. The chosen source amplitude should establish a shear flow around one order of magnitude higher than $\overline{\gamma}_{lin}$ (i.e. $\omega_{E\times B} \approx 10\overline{\gamma}_{lin}$) to fullfil the previously discussed stabilizing conditions, consistently with previous studies [38].

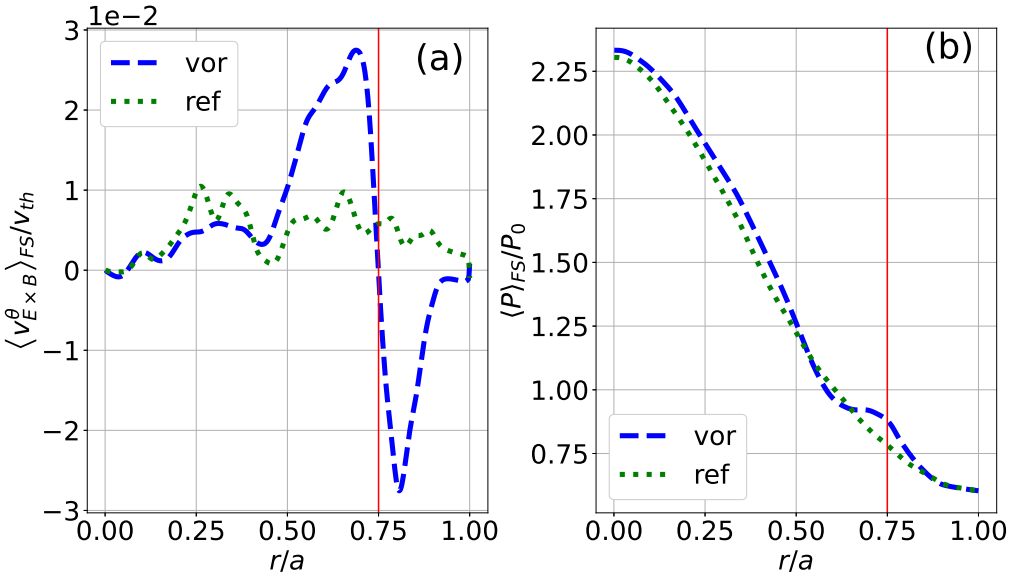

Figure 4: $E \times B$ velocity **(a)** and pressure **(b)** radial profiles of the vorticity (dashed blue line) and reference (dotted green line) cases at $t\omega_{c,0} = 377920$. The red vertical line represents the vorticity source position if activated.

Figure 4b shows the radial pressure profiles of the reference (dotted green line) and vorticity (dashed blue line) cases at the same simulation time. Three main features appear when the source is turned on: a "plateau" appears at $r/a = [0.6, 0.7]$ and the core pressure slightly increases compared to the reference case. Also, a steepening of the

pressure gradient is observed on the inner side of the plateau ($r/a = 0.6$) and on the outer side of the source ($r/a = 0.8$). One must note that in the plateau region, the $\partial_t P$ term is not negligible in the heat flux balance. This means the radial pressure profile is still evolving and may be transient. The vorticity source used here does not inject energy in the system, and the core heat source is the same as the reference case which means that the increase seen on the radial profile should result from the presence of some transport barrier.

As attested by [38], it should be noted that the vorticity source activation leads to a pressure (and therefore temperature) anisotropy that tends to destabilize the plasma and any transport barrier that could be generated by the vorticity source through quasi-periodic relaxations. This reduces locally the ITG linear threshold [54] and triggers ITG modes excitation. In previous study, this ITG modes excitation by temperature anisotropy led to periodic transport barrier crashes and consequently anisotropy collapses. However, those crashes are not observed here while a much higher temperature anistropy than previous studies is observed. A scan in collisionality at lower resolution (not shown) shows that both temperature anisotropy and shear rate saturate at a value that is independent of $\nu^\star$. The saturation value only depends on the vorticity source amplitude. Conversely, in the absence of collisions, there is no sign of saturation in the time interval that is considered, so that both temperature anisotropy and shearing rate increase to very large values. However, we did not observe the relaxation events reported by [39] possibly because of a too short simulation. The main hypothesis for the absence of relaxations is then linked to the recently upgraded collision operator used in this study [42]. Previously, only the parallel direction $v_\parallel$ was taken into account for the collisions as presented in [55], whereas the latest version takes into account the perpendicular direction μ. The derivatives in μ are then acting as an isotropizing mechanism counterbalancing the anisotropizing effect of the source, hence no relaxation mechanisms are observed in our simulations.

To quantify the effect of velocity shearing on turbulent heat transport of the main species and confinement, we choose to diagnose first the evolution of the effective heat diffusivity coefficient χ_T as a function of time in different radial regions. For this purpose, heat transport is assumed to be mainly diffusive, with the heat flux expressed as $Q = -n\chi_T \nabla T$. The radial fluxes of energy then writes:

$$Q^{neo} = \left\langle \int \mathcal{E} \left(v_D^r + v_{E_{n=0}}^r \right) \bar{F}_s dv \right\rangle_{FS}, \tag{11}$$

$$Q^{turb} = \left\langle \int \mathcal{E} \left(v_{E_{n\neq 0}}^r \right) \bar{F}_s dv \right\rangle_{FS}, \tag{12}$$

where $\mathcal{E} = \mu B + \frac{1}{2} v_{G\parallel}^2$, $v_D^r = \bar{\mathbf{v}}_D \cdot \nabla r$, $v_{E_{n=0}}^r = \langle \bar{\mathbf{v}}_{E\times B} \cdot \nabla r \rangle_\varphi$ and $v_{E_{n\neq 0}}^r = \bar{\mathbf{v}}_{E\times B} \cdot \nabla r - v_{E_{n=0}}^r$. Q^{neo} is the neoclassical heat flux, which is the sum of the curvature and gradient drift contributions as well as the toroidally axisymmetric $E\times B$ drift contribution. The turbulent heat flux Q^{turb} consists of the non toroidally axisymmetric $E \times B$ drift contribution.

The total radial heat flux is then the sum of the turbulent and neoclassical contributions:

$$Q_{tot} = Q^{turb} + Q^{neo}. \tag{13}$$

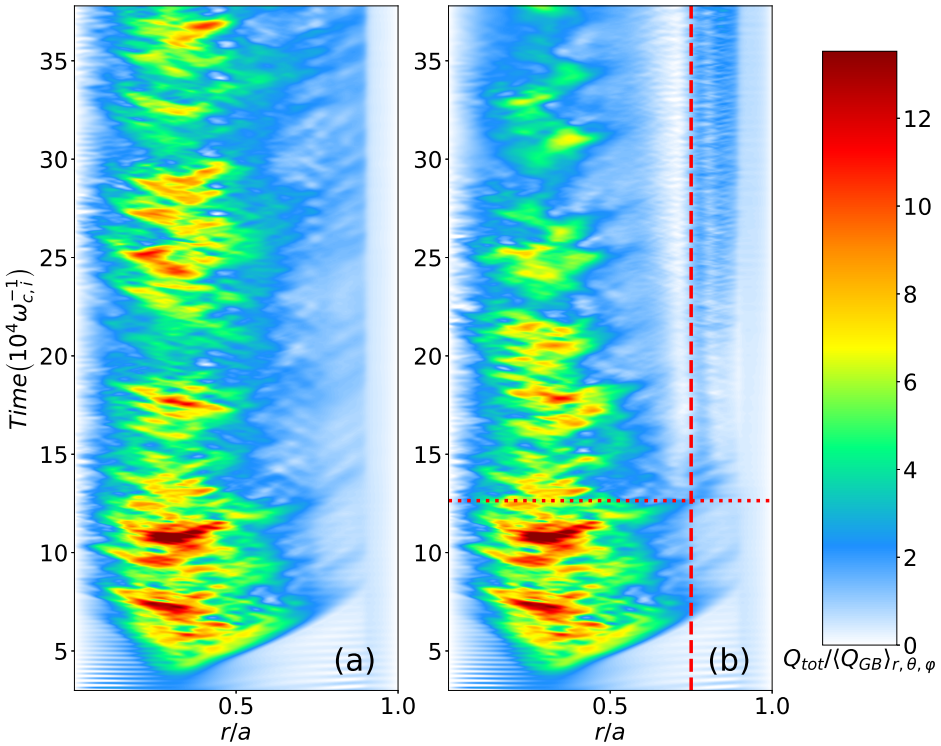

Figure 5: Total radial heat flux Q_{tot} (equation 13) as a function of radius and time for the reference **(a)** and vorticity **(b)** cases. The vertical dashed red line represents the vorticity source position while the horizontal dotted red line is the vorticity activation time.

Figure 5 represents the total radial heat flux (equation 13) as a function of radius and time normalized to the average gyro-Bohm heat flux $\langle Q_{GB}\rangle_{r,\theta,\varphi} = \langle -n_{e,0}\chi_{GB}\nabla T_{e,0}\rangle_{r,\theta,\varphi}$ with $\chi_{GB} = \rho^{\star}\chi_B = \rho^{\star}\frac{T_{e,0}}{q_i B}$, the gyro-Bohm diffusivity [56] and $T_{e,0}(r)$ and $n_{e,0}(r)$ the initial electron temperature and density profiles. After the vorticity source is activated (i.e. $15000\omega_{c,i}^{-1}$ as shown on figure 5b), a clear reduction in total heat flux is observed compared to the reference (figure 5a) case. The core region ($r/a = [0.25, 0.45]$) shows lower levels of heat flux than the reference case, which explains the higher core pressure, whereas a region of $Q_{tot} \approx 0$ arises on the inner side of the source ($r/a \in [0.6, 0.7]$) hence the plateau in the pressure profile. One can note higher heat flux levels on the outer side of the source ($r/a \in [0.75, 0.85]$) due to both the previously discussed excitation of ITG modes driven by the source-induced pressure anisotropy and the increased temperature gradient. This leads to the steepening of the pressure profile observed previously. To complete those observations, a radial average is performed on equation 13 to get such:

$$\langle Q_{tot}\rangle_{\Delta r} = \left\langle Q^{turb}\right\rangle_{\Delta r} + \langle Q^{neo}\rangle_{\Delta r}\,. \tag{14}$$

Assuming diffusive heat fluxes, one can define the different heat diffusivity components as follows:

$$\chi_T^{neo} = -\frac{\langle Q^{neo} \rangle_{\Delta r}}{\langle n \nabla T \rangle_{\Delta r}}, \tag{15}$$

$$\chi_T^{turb} = -\frac{\langle Q^{turb} \rangle_{\Delta r}}{\langle n \nabla T \rangle_{\Delta r}}, \tag{16}$$

$$\chi_T^{tot} = \chi_T^{turb} + \chi_T^{neo}. \tag{17}$$

The heat diffusivity coefficients are normalized to the local $\langle \chi_{GB} \rangle_{\Delta r,\theta,\varphi}$ gyro-Bohm diffusivity coefficients. For this analysis, we select two radial regions:

- $\Delta r = [0.7, 0.8]$, the region where the flow shear is injected.
- $\Delta r = [0.15, 0.6]$, the region where the turbulence amplitude is found maximum.

Figures 6a and 6b show the time evolution of the turbulent spatial-averaged diffusivity coefficients in the core (figure 6a) and source (figure 6b) regions respectively. The turbulent diffusivity $\chi_T^{turb} / \langle \chi_{GB} \rangle_{\Delta r,\theta,\varphi}$ quickly drops by a factor of about 10 in the vorticity source region (figure 6b, dashed blue line) when the poloidal momentum source is activated, compared to the reference simulation (figure 6b, dotted green line). In the source region, the turbulent diffusivity is the dominant factor until the vorticity source is activated. Then, the neoclassical diffusivity χ_T^{neo} becomes the dominant contribution and stays constant in both the source and core regions at approximately $\chi_T^{neo} / \langle \chi_{GB} \rangle_{\Delta r,\theta,\varphi} \approx 0.5$ for both cases. Interestingly, the turbulent diffusivity in the core is affected by the activation of the source (figure 6a, dashed blue line) even if it is not as impactful as near the source itself. An overall decaying trend seems to take place especially after the source activation. This decrease in diffusivity at the source position explains the observed pressure increase in the core as less energy is lost to the edge; this attests that a transport barrier has developed at the source location.

One can estimate the shear rate threshold above which turbulence is suppressed by checking the evolution of the turbulent diffusivity χ_T^{turb} relative to the shear rate $\omega_{E\times B}$ (figure 7). This threshold, defined as the shear rate for which $\chi_T^{turb} / \langle \chi_{GB} \rangle_{\theta,\varphi,\Delta r}$ is inferior or equal to half of its average value before the source actiavtion, is $\langle \omega_{E\times B} \rangle_{\theta,\varphi,\Delta r}^{threshold} \approx \overline{\gamma}_{lin}$, consistently with the rule of thumb discussed previously.

The observed reduction in $\langle Q^{turb} \rangle_{\Delta r}$ (see equation 14) can be explained through non-linear arguments. Let us consider a simple expression for the radial turbulent heat flux with $Q^{turb} = \langle P u^r_{E\times B} \rangle_{FS}$ with $P = (n + \delta n)(T + \delta T)$ and $\delta u^r_{E\times B} \approx \frac{1}{B_0 r} \partial_\theta \delta\phi$, the δ referring to fluctuating quantities and $\delta u^r_{E\times B}$ the perturbed $E \times B$ drift velocity. Up to the second order, this leads to:

$$Q^{turb} \approx \frac{1}{B_0 r} \left[\underbrace{\langle n \rangle_{FS} \langle \delta T \partial_\theta \delta\phi \rangle_{FS}}_{conduction} + \underbrace{\langle T \rangle_{FS} \langle \delta n \partial_\theta \delta\phi \rangle_{FS}}_{convection} \right]. \tag{18}$$

The convection term is negligeable in our simulations where electrons are adiabatic, hence we won't consider this term hereafter. One can write for a given fluctuating quantity the following expression:

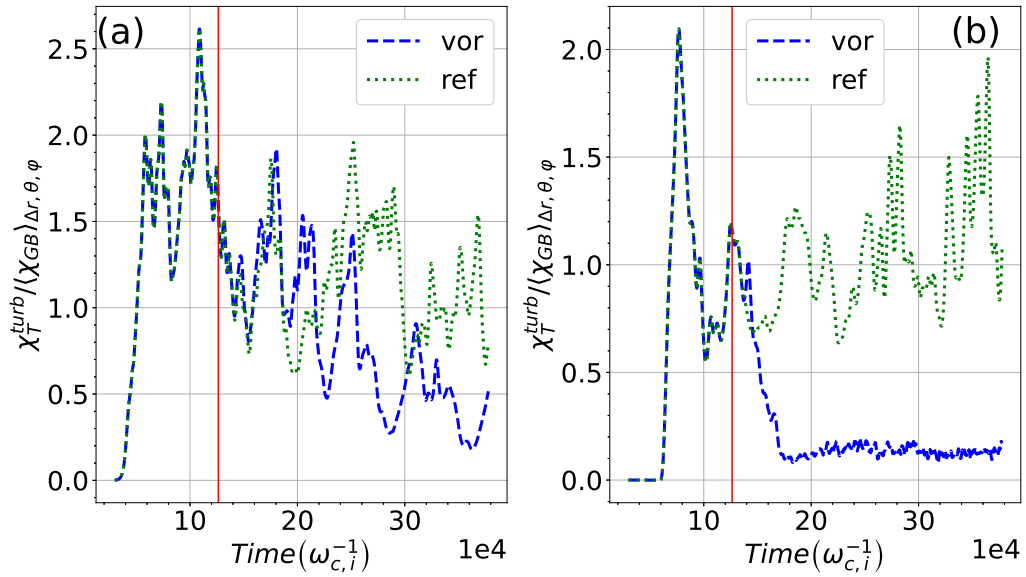

Figure 6: Time evolution of the turbulent heat diffusivity in the $r/a = [0.15, 0.6]$ **(a)** and $r/a = [0.7, 0.8]$ **(b)** regions for the vorticity (blue dashed line) and reference (dotted green line). The red vertical line represents the vorticity activation time for the vorticity case. The neoclassical diffusivity being almost constant in time, it is not presented here.

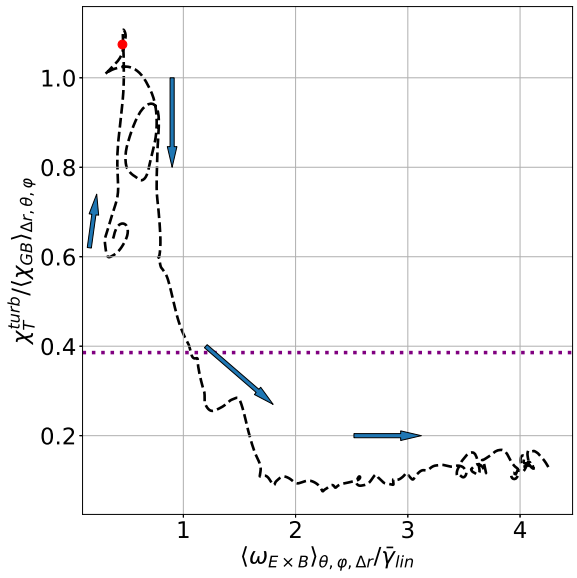

Figure 7: Turbulent heat diffusivity χ_T^{turb} plotted against the shear rate $\omega_{E\times B}$ in the source region $r/a = [0.7, 0.8]$ for $t\omega_{c,0} = [110400, 243200]$. The red dot represents the vorticity activation time for the vorticity case $t_{vor}\omega_{c,0} = 126400$. The arrows indicate the time evolution. The dotted horizontal line represents half of the maximum value of $\chi_T^{turb}/\langle\chi_{GB}\rangle_{\Delta r,\theta,\varphi}$, the threshold for turbulence suppression.

$$\delta A = \sum_{m,n} \tilde{A}_{m,n}(r) \exp\left[i\left(m\theta + n\varphi - \omega t + \Omega_A\right)\right]. \tag{19}$$

where $\tilde{A}_{m,n}(r)$ is the amplitude profile (real), m and n the poloidal and toroidal wavenumber respectively and Ω_A the phase of the quantity considered. When applied to equation 18, on can write

$$Q^{turb} \approx \frac{\langle n \rangle_{FS}}{B_0} \sum_{m,n} k_\theta \tilde{\phi}_{m,n} \tilde{T}_{m,n} \sin\left(\Omega_\phi - \Omega_T\right) \tag{20}$$

with $k_\theta = m/r$ the poloidal wavenumber. Ultimately, we consider fluctuations with similar amplitudes such as $\tilde{\phi}_{m,n} \sim \tilde{n}_{m,n} \sim \tilde{T}_{m,n}$, leading to:

$$Q^{turb} \approx \frac{\langle n \rangle_{FS}}{B_0} \sum_{m,n} k_\theta \tilde{\phi}^2_{m,n} \sin\left(\Omega_\phi - \Omega_T\right). \tag{21}$$

Equation (21) implies that Q^{turb} is proportionnal to $\tilde{\phi}^2_{m,n}$, k_θ and to the phase difference between the potential and the temperature. If the analysis presented here holds, both turbulence intensity and radial turbulent heat flux must be in phase. To verify this hypothesis, the following definition of electrostatic potential fluctuations is used:

$$\delta\phi(r,\theta,\varphi=0,t) = \phi(r,\theta,\varphi=0,t) - \langle \phi(r,\theta,\varphi) \rangle_\varphi, \tag{22}$$

$\langle \phi(r,\theta,\varphi) \rangle_\varphi$ represents the toroidally axisymmetric modes of the potential and are substracted specifically to remove the contribution coming from :

- The mean potential, or the so-called $\phi_{0,0}$ Fourier mode, which is related to zonal flows [57].
- The convection cells [57], which are toroidally axisymmetric but exhibit poloidal asymetries. They are associated with the $\phi_{m\neq 0,0}$ Fourier components.

The focus here is on a single poloidal plane $(r,\theta,\varphi=0)$ representative of the whole simulation box. Information of interest being the local turbulence intensity and later the radial and poloidal geometric structures, this will provide sufficient information on those variables as discussed in [58] and [59]. The local radial turbulence intensity is then computed by averaging the square of equation (22) over θ and Δr:

$$I_{turb} = \left\langle \left[\delta\phi(r,\theta,\varphi=0,t)\right]^2 \right\rangle_{\theta,\Delta r}. \tag{23}$$

I_{turb} is normalized to I^{max}_{turb}, the maximum value reported before the source activation which is the same for both the reference and vorticity cases. Figures 8 and 9 represent the time evolution of the turbulent heat flux and turbulence intensity in the source (figure 8) and core (figure 9) regions respectively. As expected, I_{turb} and $\left\langle Q^{turb} \right\rangle_{\Delta r}$ are in phase in both regions, implying the previous relationship found between Q^{turb} and $I_{turb} \leftrightarrow \tilde{\phi}^2$ holds

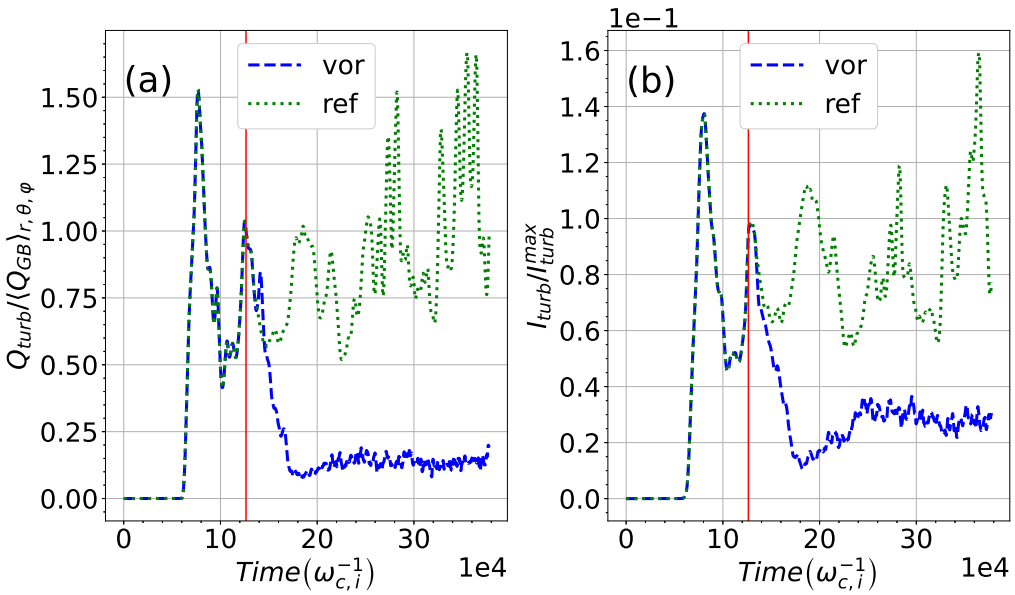

Figure 8: Time evolution of the turbulence heat flux **(a)** and turbulent intensity **(b)** in the $r/a = [0.7, 0.8]$ region for the vorticity (blue dashed line) and reference (dotted green line). The red vertical line represents the vorticity activation time for the vorticity case. **(a)** and **(b)** signals are in phase.

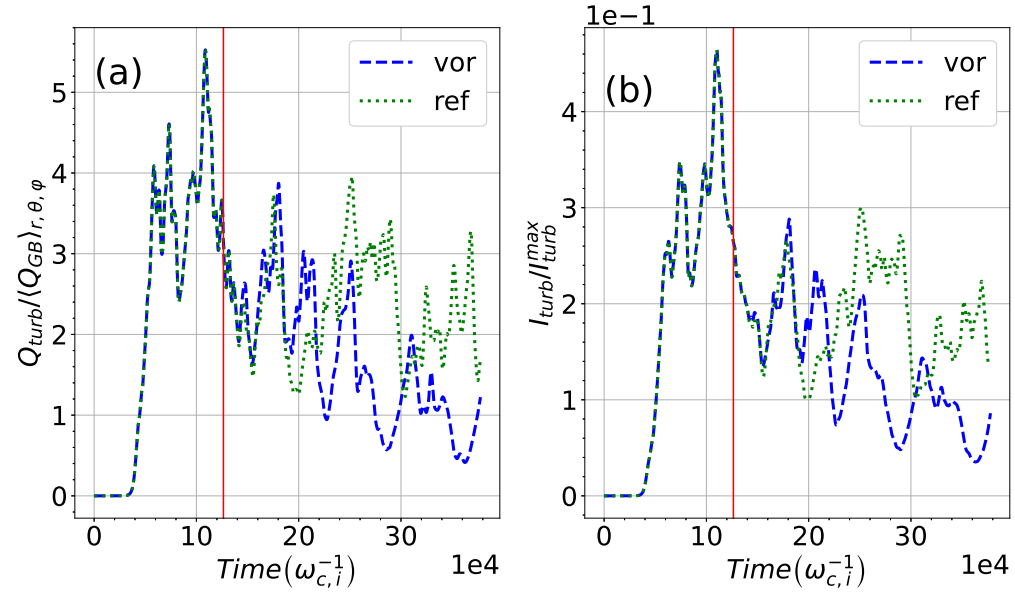

Figure 9: This figure shows the time evolution of the turbulent heat flux **(a)** and turbulence intensity **(b)** in the $r/a = [0.15, 0.6]$ region for the vorticity (blue dashed line) and reference (dotted green line) cases. The red vertical line represents the vorticity activation time for the vorticity case. **(a)** and **(b)** signals are in phase.

in the case of adiabatic electrons. When the vorticity source is activated, the turbulence intensity largely decreases in the source region by a factor 3 while heat flux decreases by a factor 10. Note that there is still a small turbulence level present locally. Moreover, the turbulence intensity also decreases in the core (figure 9) when the vorticity source is on. The reduction in turbulent heat flux is then directly linked to the reduction of turbulence intensity.

Another way to verify the validity of the relation described in equation (21) is to plot $\left\langle Q_{tot}^{turb} \right\rangle_{\Delta r}$ as a function of I_{turb} in the core (figure 10a) and source regions (figure 10b). A linear fit $Q_{turb}/\left\langle Q_{GB} \right\rangle_{r,\theta,\varphi} = aI_{turb}/I_{turb}^{max}$ is then applied to the data to check the validity of equation (21). In the source region, both the turbulence intensity and turbulent heat flux in the vorticity case are at very low levels compared to the reference case. However, the fit for the reference case is more robust ($R^2 = 0.57$) with a slope of $a_{source}^{ref} \sim 11.2$ while it's only $a_{source}^{vor} \sim 4.8$ in the vorticity case ($R^2 = 0.09$). Not withstanding the small value of the R^2 value in the vorticity case, it is appearant that the plasma behaviour is different than in the reference case. This indicates large variations in k_θ and/or phase differences. In the core region, both the reference and vorticity cases show similar slopes of $a_{core}^{vor} \approx a_{core}^{ref} \sim 12.5$ with a convincing determination coefficient $R^2 > 0.8$. This means the turbulence has similar features but with a lower amplitude when the vorticity is on and verifies equation (21).

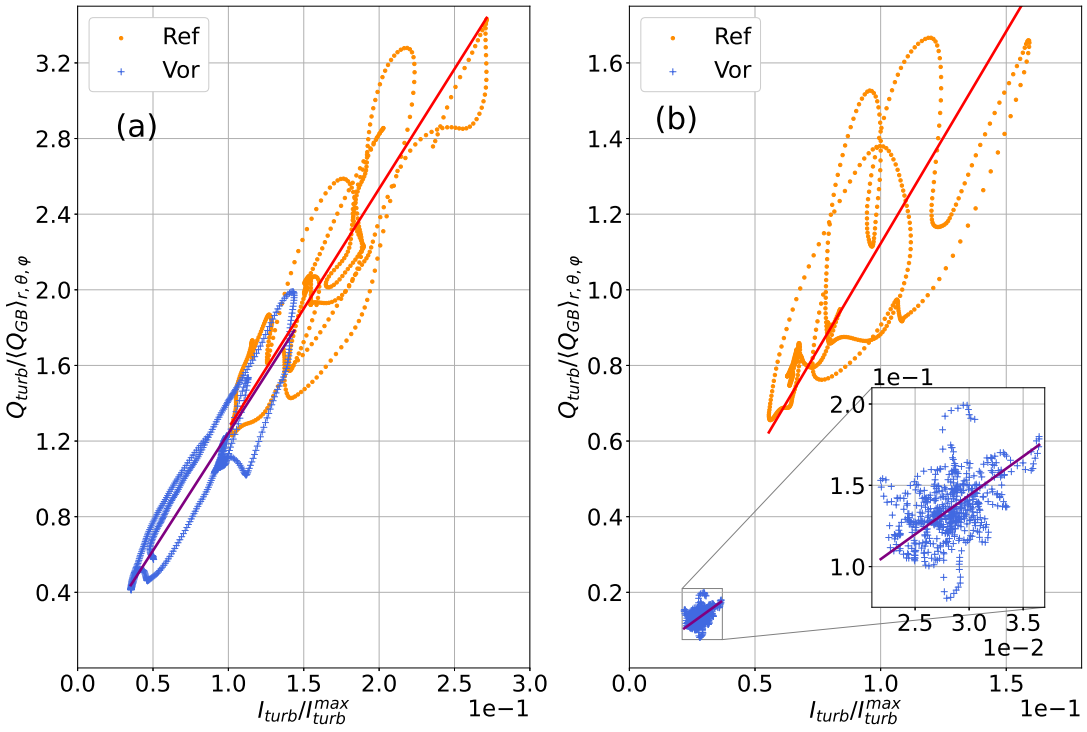

Figure 10: Heat flux as a function of turbulence intensity for the vorticity (blue cross) and reference (orange dots) cases in the core **(a)** and source **(b)** regions.

4.2 Involved mechanisms: auto-correlation length and perpendicular wavenumber

As already discussed in the introduction, one of the main hypothesis is that an $E \times B$ flow shear is able to *tear* the turbulent structures locally to reduce their mean size and therefore stabilize the plasma. We propose two different approaches to verify this prediction in our simulations:

1. Compute and compare the local auto-correlation radial length of the perturbed electrostatic potential for both the reference and vorticity cases. The aim is to check any change in typical radial structure size.

2. Compute the poloidal wavenumber spectrum of the perturbed electrostatic potential to monitor what poloidal scales are specifically affected by this turbulence intensity quench.

4.2.1 Auto-correlation radial length

The aim in this paragraph is to quantify effect on the "mean" size of turbulent structures of the $E \times B$ shear flow. For this purpose, we calculate the fluctuations as written in equation (22) and then compute a correlation length Probability Density Function (PDF), following reference [58]:

$$C_{\delta\phi,\delta\phi}\left(r,\theta,\varphi=0,t,\delta r\right)=\frac{\delta\phi\left(r+\delta r,\theta,\varphi=0,t\right)\delta\phi\left(r,\theta,\varphi=0,t\right)}{\left[\delta\phi\left(r,\theta,\varphi=0,t\right)\right]^{2}} \tag{24}$$

This autocorrelation function is computed for each θ angle and radial location r on a radial window $[r-\delta r_{max}, r+\delta r_{max}]$. Here we adjust the radial extent to $\delta r_{max}=20\rho_{c,0}$, which is found to be sufficient to capture most of the turbulent radial structures. Thus we obtain a PDF for each time step, θ angle and radius $r/a \in [0.1, 0.9]$. The Half Width at Half Maximum (HWHM) of this PDF is taken along δr to obtain a time dependent poloidal map of the radial correlation length:

$$C_{\delta\phi,\delta\phi}\left(r,\theta,\varphi=0,t,L_{AC}^{\delta\phi}\right)=0.5. \tag{25}$$

Finally, the flux-surface average of the poloidal map obtained is computed before doing a time average over the last $48000t\omega_{c,0}$ of both the simulation an reference cases.

$$\left\langle L_{AC}\right\rangle_{FS}\left(r\right)=\overline{\left\langle L_{AC}^{\delta\phi}\left(r,\theta,t\right)\right\rangle_{FS}}, \tag{26}$$

with the overline representing the time average.

Figure 11a shows the flux-surface and time averaged auto-correlation length as a fuction of the normalized radius while figure 11b shows the radial profile of the shear rate $\omega_{E\times B}$ at the last simulation time. The reference case (figure 11a, dotted green line) represents the correlation length without the vorticity source. L_{AC} stays close to $3.5\rho_{c,i}$ with a small $E \times B$ shear rate (figure 11b, dotted green line), but if the source is turned on

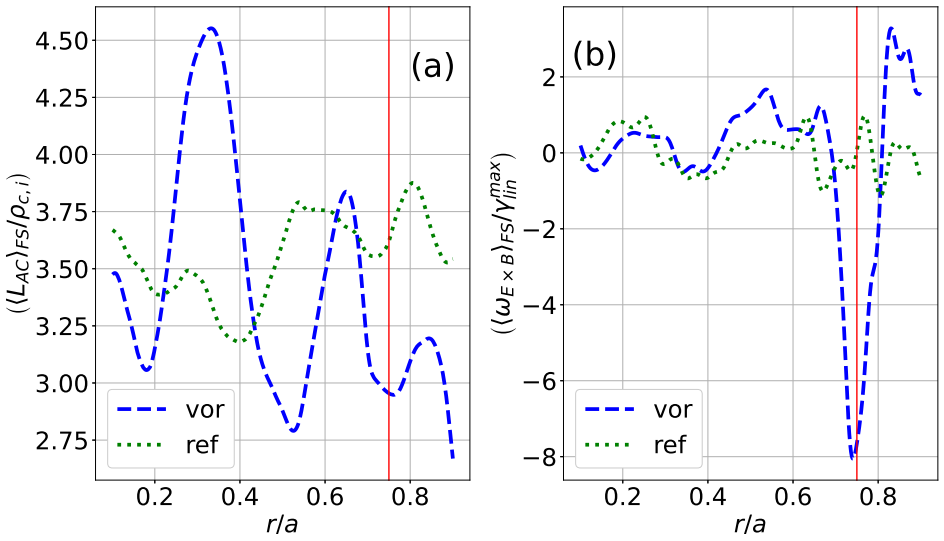

Figure 11: Flux surface and time average of the correlation length normalized to the local ion gyro-radius **(a)** and $E \times B$ shearing rate **(b)** as a function of radius for the reference (green dotted line) and vorticity (blue dashed line) cases. The red vertical line indicates the source location for the vorticity case.

(figure 11a, dashed blue line), the radial correlation decreases where the flow shear rate is maximum (figure 11b, dashed blue line), at $r/a = 0.75$. This is consistent with the turbulent structure shearing hypothesis: the $E \times B$ shear flow reduces locally the radial extension of the turbulent structures. This ultimately leads to a spatial decorrelation of those structures and a quench in turbulence intensity as previously observed. Conversely, the correlation length increases in the range $r/a \in [0.2; 0.4]$ and decreases near $r/a = 0.5$ where shearing is not strong. Hence, the decrease of χ_T and of the turbulence intensity in those regions cannot be attributed to the auto-correlation length.

4.2.2 Poloidal wavenumber spectra

To complete this analysis, we compute the k_θ spectrum of the perturbed electrostatic potential to monitor the intensity evolution of the different poloidal structure scales at different radii. The k_θ spectrum is computed through

$$|\delta\phi_{k_\theta}|^2 (r, k_\theta) = \overline{|\delta\phi (r, k_\theta, \varphi = 0, t)|^2}. \tag{27}$$

For each time step, a 1D FFT is performed along the poloidal axis before averaging it over the last $48000 t\omega_{c,0}$ to get a cleaner signal. This is comparable to $\left|\delta\phi^{3D}_{k_\theta}\right|^2 (r, k_\theta) = \overline{\sum_{k_\varphi} |\delta\phi (r, k_\theta, k_\varphi)|^2}$ because the dominant modes are the resonant ones.
Figure 12a shows the core region (i.e. $r/a = 0.43$) poloidal wavenumber spectra for the reference case (dotted green line) and vorticity case (dashed blue line). The vorticity case spectrum keeps the same features as the reference one with a slightly lower amplitude. Figure 12b shows the poloidal wavenumber spectrum for the source region (i.e. $r/a = 0.75$). A clear difference can be seen between the reference (dotted green line) and vorticity case (dashed blue line). The smallest poloidal scales ($k_\theta \rho_{c,i} > 0.1$) undergo a much more important decrease in intensity than the bigger scales ($k_\theta \rho_{c,i} < 0.1$). This shows a reorganisation of the turbulent structures at that location with a mean scale shifting

from $\overline{k_\theta \rho_{c,i}} \approx 0.28$ to $\overline{k_\theta \rho_{c,i}} \approx 0.16$, meaning the poloidal structures got bigger but also less intense. One explanation for this local shift is that turbulent structures may get *tilted* along the poloidal direction due to shearing as shown in figure 1 of [53]. As a result turbulent structures are radially smaller and poloidally bigger with an overall lower intensity.

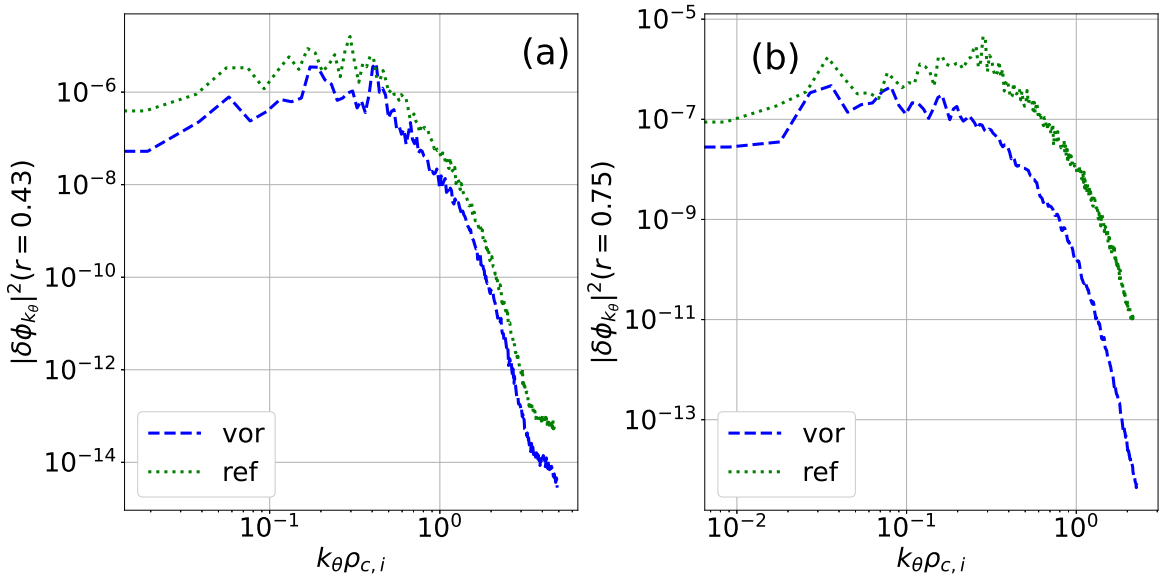

Figure 12: Poloidal wavenumber spectra using a 1D FFT averaged over the last 100 time steps for the reference (green dotted line) and vorticity (blue dashed line) cases for $r/a = 0.43$ **(a)** and $r/a = 0.75$ **(b)**.

5 Steep gradient case

Another way to generate a localized $E \times B$ poloidal shear flow is to produce a radially strong pressure gradient (figure 13a) as shown with the radial density profile on figure 2a. Since the temperature profile is allowed to evolve (flux-driven condition) but not the ion density profile (adiabatic electrons), we can enforce an initial density profile with a steep gradient at the desired location, the pressure gradient intensity defining the poloidal shear flow amplitude. The main interest of this approach is to determine how the heat transport coefficients behave when an H-mode pressure profile is enforced from the start. A simulation with such gradient and characteristics detailed in table 1 shows that this method creates indeed the desired radial profile of poloidal $E \times B$ shear flow as shown in figure 13b. Notice that, in this case, the velocity profile is different from the vorticity-induced one (figure 4b, dashed blue line) with a single lobe instead of two at $r/a = 0.75$. Outside of the steep gradient region, the $E \times B$ velocity profile is similar to what is observed in the reference case.

Figure 14 shows the time evolution of the total heat diffusivity (figure 14a), the turbulent heat flux (figure 14b) and the turbulent intensity (figure 14c) in the steep gradient region. The turbulent diffusivity is vanishing in that region and only marginally contributes to the total diffusivity now dominated by the neoclassical coefficient, roughly constant at $\chi_T^{neo} / \langle \chi_{GB} \rangle_{\Delta r,\theta,\varphi} \approx 0.5$. The radial turbulent heat flux (figure 14b) shows

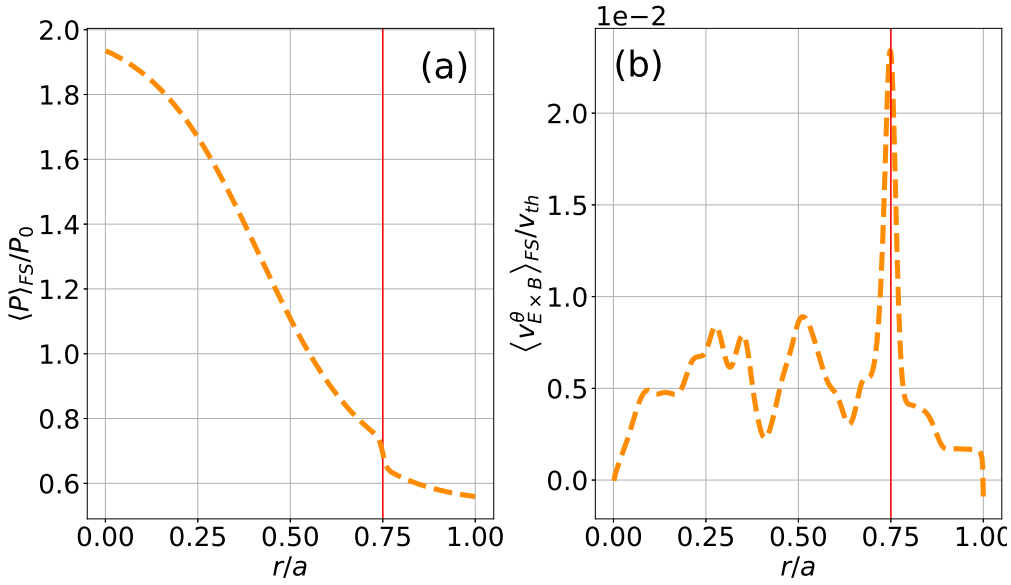

Figure 13: Radial profile of the total pressure **(a)** and $E \times B$ poloidal velocity **(b)** at the simulation end for the steep gradient case. The red vertical line indicates the steep gradient position.

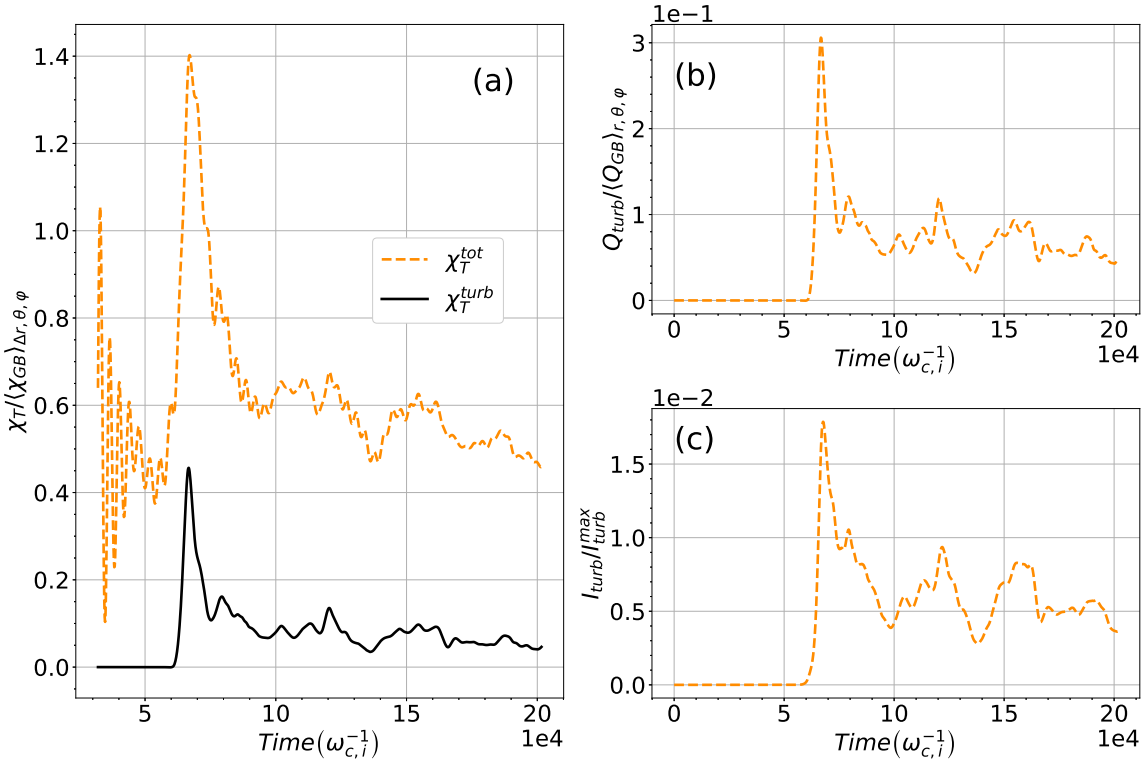

Figure 14: Diffusivity, turbulent heat flux and turbulence intensity time evolution averaged in the $r/a = [0.7, 0.8]$ region for the steep gradient case. **(a)** Time evolution of the total (dashed orange line) and turbulent (solid black line) heat diffusivity coefficient. **(b)** Turbulent heat flux as a function of time. **(c)** Turbulence intensity plotted against time. **(b)** and **(c)** signals are in phase.

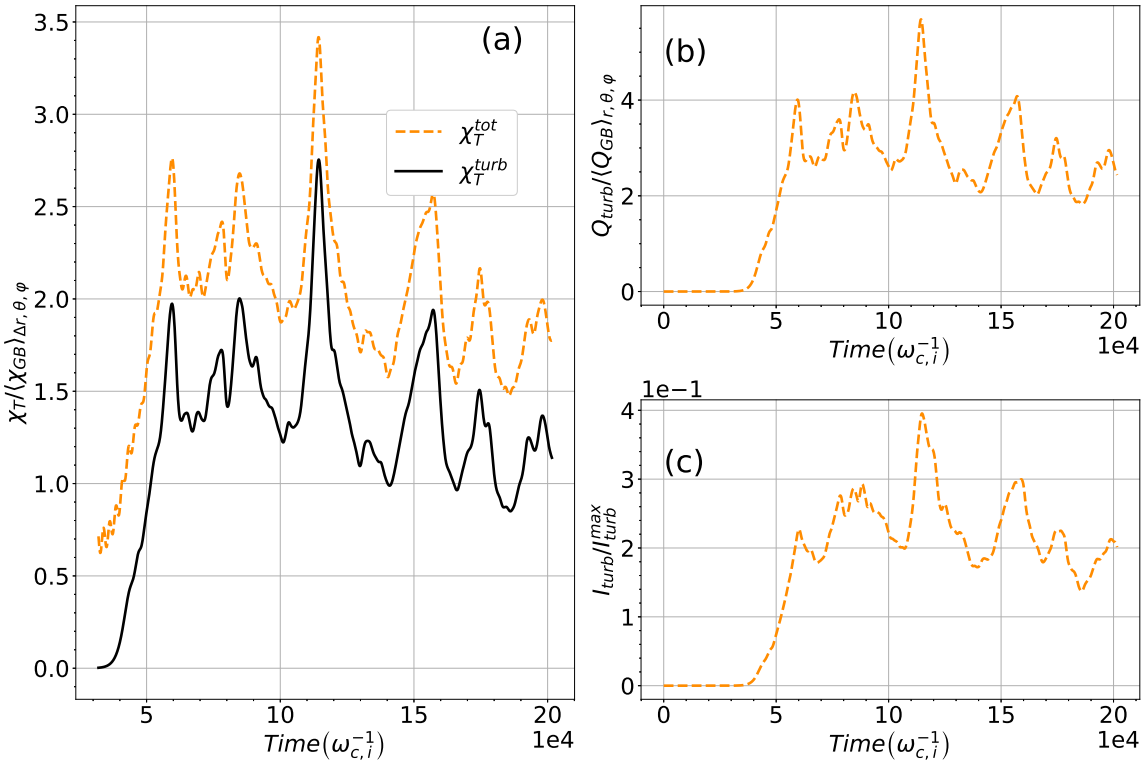

Figure 15: This figure is similar to figure 14 except that the radial average is in the $r/a = [0.15, 0.6]$ region for the steep gradient case. **(a)** Time evolution of the total (dashed orange line) and turbulent (solid black line) heat diffusivity coefficient. **(b)** Turbulent heat flux as a function of time. **(c)** Turbulence intensity plotted against time. **(b)** and **(c)** signals are in phase.

the same trend as the turbulence intensity (figure 14c) and drops to very low levels even smaller than the level observed in the vorticity case (8a).

In the core, the diffusivity is dominated by tubulence and does not show the decaying trend (figure 15a). Figure 15b shows the time evolution of the radial turbulent heat flux which again correlates strongly with the turbulence intensity in the same region (figure 15c). This approach seems effective to reduce the heat turbulent transport coefficient and turbulence intensity both near the steep gradient and in the core.

The origin of the barrier is however more ambiguous than in the vorticity case. Two main factors need to be taken into account here. The first one is the linear stabilization of ITG by the density gradient. The criteria to enable ITG to grow linearly in a tokamak geometry is given in [60]. With our parameters, we get $\kappa_T^{crit} = 22.4$, which is higher than the prescribed value of $\kappa_T = 6.6$. Therefore, the linear stabilization of ITG modes by the density gradient is primarly responsible for the transport barrier creation and the low turbulent heat flux observed in the region $r/a = [0.7, 0.8]$.

Moreover, one cannot neglect the impact of the $E \times B$ shear flow generated by the pressure gradient. As shown on figure 11b and 16b, the shearing levels generated by the source and the steep gradient present different shapes (i.e. two vs one lobe) but are within the same order of magnitude of $\sim 8\bar{\gamma}_{lin}$, the average linear growth rate of ITG modes at $r/a = 0.5$. The $E \times B$ flow shear is likely to prevent ITG turbulence to propagate across this region by tearing appart convective cells that could develop e.g. through turbulence spreading. This results in an even more "effective" transport barrier with two different stabilizing mechanisms taking place simultaneously.

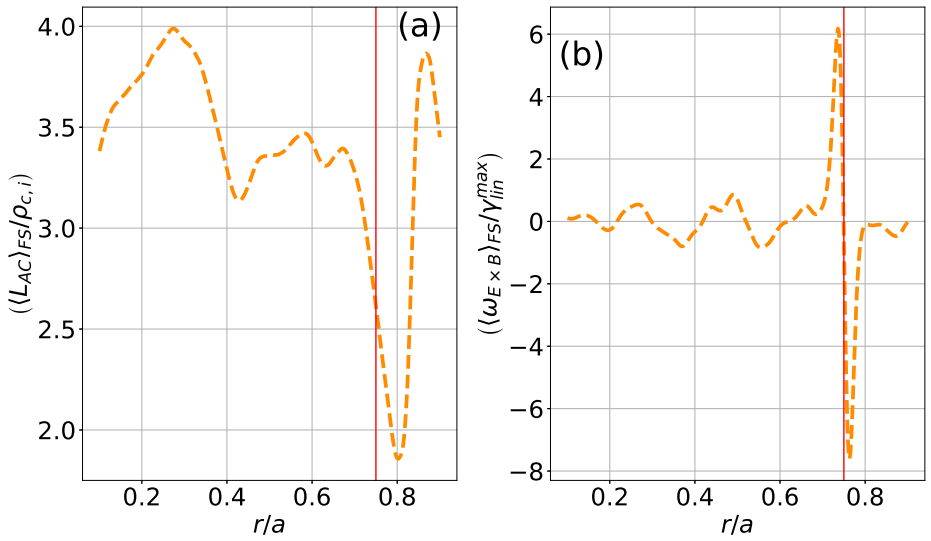

Figure 16: Flux surface and time average of the correlation length **(a)** and $E \times B$ shearing rate **(b)** as a function of radius for the steep gradient case. The red vertical line indicates the steep gradient location.

Figure 16a confirms the previous analysis by showing that the auto-correlation radial length of the perturbed potential is significantly lower near the steep gradient position at $r/a = 0.75$. This shows that almost no turbulence structures are present here while the rest of the plasma manifests a similar behaviour as evidenced in the reference case (figure 11b, dotted green line).

6 Discussion and conclusion

We have analyzed here, by means of flux driven gyrokinetic simulations of ITG turbulence, two different ways to reduce turbulence and make the plasma bifurcate to what can be described as an improved confinement mode with the development of a transport barrier.

The first way is based on a method proposed by A. Strugarek [38] [39] that uses a vorticity source to locally polarize the plasma and generate a strong $E \times B$ shear flow comparable to what is observed experimentally for such plasmas. This method leads to the effective reduction of the turbulent heat diffusivity χ_T^{turb} in the source region when the shear rate $\omega_{E\times B}$ reaches a threshold of $\omega_{E\times B} \approx \overline{\gamma}_{lin}$, meaning no fluctuation persists in the vicinity of the strongly sheared region. A minor reduction in χ_T^{turb} is observed as well in the core region compared to a reference case, showing that the edge-localized source has an impact on the core. This reduction in turbulent transport can be explained by the turbulence intensity quench observed when vorticity is turned on. Moreover, a shearing of the larger turbulent structures into smaller ones is observed as attested by the change of correlation length in the strong flow shear region. The k_θ spectrum analysis shows the impact of the source with lower turbulence intensity, shifting the maximum of the spectrum to the lower wavenumbers. This effect is due to the structures being tilted in the poloidal direction. This reduction in heat transport led to slightly higher pressure in the core than the reference scenario without the vorticity source.

The second way consists in enforcing a H-mode-like density profile to generate through the radial force balance a localized strong $E \times B$ shear flow. This alternative method managed to stabilize the plasma locally by linearly stabilizing ITG modes through the steep gradient profile enforced. In addition to this linear stabilization effect, the $E \times B$ flow shear generated by the steep pressure gradient also helps stabilizing the plasma by tearing apart any turbulent structures that could grow in the steep gradient region. The edge reduction in heat transport leads to higher core temperatures, meaning the created transport barrier is efficient enough to increase energy confinement.

Accounting for kinetic electrons would allow particle transport in the simulation presented here in both the vorticity and steep gradient cases. The latter case would therefore be difficult to study as we expect the enforced steep density gradient to collapse rapidly and it is not expected to generate and maintain a transport barrier. In addition, TEMs would arise in the system and combine with ITGs and probably lead to higher turbulence level since steep density gradients are destabilizing for TEMs [61]. We still expect the vorticity source to be relevant in the presence of kinetic electrons and we expect a transport barrier could still arise in those conditions, even with TEMs.

However, one may expect a different threshold in the magnitude of the vorticity source to trigger a transport barrier. Indeed, the saturation of TEM turbulence exhibits a different sensitivity to Zonal Flows as compared to ITG. In particular, their contribution to TEM saturation has been found to depend on local plasma parameters, most critically the temperature ratio T_e/T_i and $\eta = L_n/L_{Te}$, the ratio of density over temperature gradient lengths [62][63][64][65].

The next step with this study is to inject impurities, like helium and tungsten, and observe the effect of those barriers on the impurity heat and particle transport with similar parameters in GYSELA.

Acknowledgements

This work has been carried out within the framework of the EUROfusion Consortium, funded by the European Union via the Euratom Research and Training Programme (Grant Agreement No 101052200 — EUROfusion). Views and opinions expressed are however those of the author(s) only and do not necessarily reflect those of the European Union or the European Commission. Neither the European Union nor the European Commission can be held responsible for them. It was partly funded by the Agence Nationale de la Recherche for the project GRANUL (ANR-19-CE30-0005). This work was also supported by funding from the European Union's Horizon 2020 research and innovation program under grant agreement no. 824158 (EoCoE II). This work was granted access to the HPC resources of IDRIS under special allocation spe00012 made by GENCI and of MARCONI under project FUA35 GSNTITE .

References

[1] F. Hinton and R. D. Hazeltine, "Theory of plasma transport in toroidal confinement systems," *Reviews of Modern Physics*, vol. 48, no. 2, p. 239, 1976.

[2] P. C. Liewer, "Measurements of microturbulence in tokamaks and comparisons with theories of turbulence and anomalous transport," *Nuclear Fusion*, vol. 25, no. 5, p. 543, 1985.

[3] A. Wootton, B. Carreras, H. Matsumoto, K. McGuire, W. Peebles, C. P. Ritz, P. Terry, and S. Zweben, "Fluctuations and anomalous transport in tokamaks," *Physics of Fluids B: Plasma Physics*, vol. 2, no. 12, pp. 2879–2903, 1990.

[4] X. Garbet, P. Mantica, C. Angioni, E. Asp, Y. Baranov, C. Bourdelle, R. Budny, F. Crisanti, G. Cordey, L. Garzotti, *et al.*, "Physics of transport in tokamaks," *Plasma Physics and Controlled Fusion*, vol. 46, no. 12B, p. B557, 2004.

[5] R. Waltz, G. Kerbel, and J. Milovich, "Toroidal gyro-Landau fluid model turbulence simulations in a nonlinear ballooning mode representation with radial modes," *Physics of Plasmas*, vol. 1, no. 7, pp. 2229–2244, 1994.

[6] W. Tang, G. Rewoldt, and L. Chen, "Microinstabilities in weak density gradient tokamak systems," *The Physics of fluids*, vol. 29, no. 11, pp. 3715–3718, 1986.

[7] P. Guzdar, L. Chen, W. Tang, and P. Rutherford, "Ion-temperature-gradient instability in toroidal plasmas," *The Physics of Fluids*, vol. 26, no. 3, pp. 673–677, 1983.

[8] G. Lee and P. Diamond, "Theory of ion-temperature-gradient-driven turbulence in tokamaks," *The Physics of fluids*, vol. 29, no. 10, pp. 3291–3313, 1986.

[9] S. C. Prager, A. Sen, and T. Marshall, "Dissipative trapped-electron instability in cylindrical geometry," *Physical Review Letters*, vol. 33, no. 12, p. 692, 1974.

[10] T. Drouot, E. Gravier, T. Reveille, A. Ghizzo, P. Bertrand, X. Garbet, Y. Sarazin, and T. Cartier-Michaud, "A gyro-kinetic model for trapped electron and ion modes," *The European Physical Journal D*, vol. 68, no. 10, pp. 1–7, 2014.

[11] N. D'Angelo, "Kelvin-Helmholtz instability in a fully ionized plasma in a magnetic field," *The Physics of Fluids*, vol. 8, no. 9, pp. 1748–1750, 1965.

[12] G. I. Kent, N. C. Jen, and F. F. Chen, "Transverse Kelvin-Helmholtz instability in a rotating plasma," *The Physics of Fluids*, vol. 12, no. 10, pp. 2140–2151, 1969.

[13] F. Wagner, G. Becker, K. Behringer, D. Campbell, A. Eberhagen, W. Engelhardt, G. Fussmann, O. Gehre, J. Gernhardt, G. v. Gierke, *et al.*, "Regime of improved confinement and high beta in neutral-beam-heated divertor discharges of the ASDEX tokamak," *Physical Review Letters*, vol. 49, no. 19, p. 1408, 1982.

[14] T. Kobayashi, "The physics of the mean and oscillating radial electric field in the L-H transition: the driving nature and turbulent transport suppression mechanism," *Nuclear Fusion*, vol. 60, no. 9, p. 095001, 2020.

[15] C. Bourdelle, "Staged approach towards physics-based L-H transition models," *Nuclear Fusion*, vol. 60, no. 10, p. 102002, 2020.

[16] Y. Yang, X. Gao, H. Liu, G. Li, T. Zhang, L. Zeng, Y. Liu, M. Wu, D. Kong, T. Ming, *et al.*, "Observation of internal transport barrier in ELMy H-mode plasmas on the EAST tokamak," *Plasma Physics and Controlled Fusion*, vol. 59, no. 8, p. 085003, 2017.

[17] J. Chung, H. Kim, Y. Jeon, J. Kim, M. Choi, J. Ko, K. Lee, H. Lee, S. Yi, J. Kwon, *et al.*, "Formation of the internal transport barrier in KSTAR," *Nuclear Fusion*, vol. 58, no. 1, p. 016019, 2017.

[18] D. Frigione, L. Garzotti, C. Challis, M. De Baar, P. De Vries, M. Brix, X. Garbet, N. Hawkes, A. Thyagaraja, L. Zabeo, *et al.*, "Pellet injection and high density ITB formation in JET advanced tokamak plasmas," *Nuclear fusion*, vol. 47, no. 2, p. 74, 2007.

[19] S. Ding, G. Xu, Q. Wang, W. Solomon, Y. Zhao, X. Gong, A. Garofalo, C. Holcomb, G. McKee, Z. Yan, *et al.*, "Scenario development for high β_p low torque plasma with q_{min} above 2 and large-radius internal transport barrier in DIII-D," *Nuclear Fusion*, vol. 57, no. 2, p. 022016, 2016.

[20] S. Ide, T. Suzuki, Y. Sakamoto, H. Takenaga, T. Fujita, N. Oyama, A. Isayama, Y. Koide, Y. Kamada, *et al.*, "studies of the influence of electron heating on ITB subject to advanced tokamak operation in JT-60U," *Nuclear fusion*, vol. 44, no. 1, p. 87, 2003.

[21] K. Burrell, S. Allen, G. Bramson, N. Brooks, R. Callis, T. Carlstrom, M. Chu, A. Colleraine, D. Content, J. DeBoo, *et al.*, "Confinement physics of H-mode discharges in DIII-D," *Plasma Physics and Controlled Fusion*, vol. 31, no. 10, p. 1649, 1989.

[22] P. Gohil, K. Burrell, and T. Carlstrom, "Parametric dependence of the edge radial electric field in the DIII-D tokamak," *Nuclear fusion*, vol. 38, no. 1, p. 93, 1998.

[23] K. Ida, S. Hidekuma, Y. Miura, T. Fujita, M. Mori, K. Hoshino, N. Suzuki, T. Yamauchi, J.-M. group, *et al.*, "Edge electric-field profiles of H-mode plasmas in the JFT-2M tokamak," *Physical Review Letters*, vol. 65, no. 11, p. 1364, 1990.

[24] R. Dermott, B. Lipschultz, J. Hughes, P. Catto, A. Hubbard, I. Hutchinson, M. Greenwald, B. Bombard, K. Marr, M. Reinke, *et al.*, "Edge radial electric field structure and its connection to H-mode confinement in Alcator C-Mod," 2009.

[25] Y. Andrew, N. Hawkes, T. Biewer, K. Crombe, D. Keeling, E. De La Luna, C. Giroud, A. Korotkov, A. Meigs, A. Murari, *et al.*, "Evolution of the radial electric field in a JET H-mode plasma," *EPL (Europhysics Letters)*, vol. 83, no. 1, p. 15003, 2008.

[26] E. Viezzer, T. Pütterich, G. Conway, R. Dux, T. Happel, J. Fuchs, R. McDermott, F. Ryter, B. Sieglin, W. Suttrop, *et al.*, "High-accuracy characterization of the edge radial electric field at ASDEX upgrade," *Nuclear Fusion*, vol. 53, no. 5, p. 053005, 2013.

[27] J. Schirmer, G. Conway, H. Zohm, W. Suttrop, *et al.*, "The radial electric field and its associated shear in the ASDEX Upgrade tokamak," *Nuclear fusion*, vol. 46, no. 9, p. S780, 2006.

[28] R. Panek, J. Adámek, M. Aftanas, P. Bílková, P. Böhm, F. Brochard, P. Cahyna, J. Cavalier, R. Dejarnac, M. Dimitrova, *et al.*, "Status of the COMPASS tokamak and characterization of the first H-mode," *Plasma Physics and Controlled Fusion*, vol. 58, no. 1, p. 014015, 2015.

[29] H. Meyer, C. Bunting, P. Carolan, N. Conway, M. Dunstan, A. Kirk, R. Scannell, D. Temple, M. Walsh, *et al.*, "The structure, evolution and role of the radial edge electric field in H-mode and L-mode on MAST," in *Journal of Physics: Conference Series*, vol. 123, p. 012005, IOP Publishing, 2008.

[30] W. Chen, L. Yu, M. Xu, Z. Shi, X. He, D. Yu, X. Ji, Y. Li, M. Jiang, P. Shi, *et al.*, "high-β_p scenario realized by the integration of internal and external transport barriers in the HL-2A tokamak," *Physics Letters A*, vol. 440, p. 128141, 2022.

[31] Z. Lin, T. S. Hahm, W. Lee, W. M. Tang, and R. B. White, "turbulent transport reduction by zonal flows: Massively parallel simulations," *Science*, vol. 281, no. 5384, pp. 1835–1837, 1998.

[32] R. L. Dewar and R. F. Abdullatif, "Zonal flow generation by modulational instability," in *Frontiers in Turbulence and Coherent Structures*, pp. 415–430, World Scientific, 2007.

[33] P. H. Diamond, S. Itoh, K. Itoh, and T. Hahm, "Zonal flows in plasma—a review," *Plasma Physics and Controlled Fusion*, vol. 47, no. 5, p. R35, 2005.

[34] S. Kobayashi, Ö. D. Gürcan, and P. H. Diamond, "Direct identification of predator-prey dynamics in gyrokinetic simulations," *Physics of Plasmas*, vol. 22, no. 9, p. 090702, 2015.

[35] H. Biglari, P. Diamond, and P. Terry, "Influence of sheared poloidal rotation on edge turbulence," *Physics of Fluids B: Plasma Physics*, vol. 2, no. 1, pp. 1–4, 1990.

[36] K. Itoh and S.-I. Itoh, "The role of the electric field in confinement," *Plasma physics and controlled fusion*, vol. 38, no. 1, p. 1, 1996.

[37] P. Terry, "Suppression of turbulence and transport by sheared flow," *Reviews of Modern Physics*, vol. 72, no. 1, p. 109, 2000.

[38] A. Strugarek, Y. Sarazin, D. Zarzoso, J. Abiteboul, A. Brun, T. Cartier-Michaud, G. Dif-Pradalier, X. Garbet, P. Ghendrih, V. Grandgirard, *et al.*, "Ion transport barriers triggered by plasma polarization in gyrokinetic simulations," *Plasma Physics and Controlled Fusion*, vol. 55, no. 7, p. 074013, 2013.

[39] A. Strugarek, Y. Sarazin, D. Zarzoso, J. Abiteboul, A. Brun, T. Cartier-Michaud, G. Dif-Pradalier, X. Garbet, P. Ghendrih, V. Grandgirard, *et al.*, "Unraveling quasiperiodic relaxations of transport barriers with gyrokinetic simulations of tokamak plasmas," *Physical review letters*, vol. 111, no. 14, p. 145001, 2013.

[40] V. Grandgirard, J. Abiteboul, J. Bigot, T. Cartier-Michaud, N. Crouseilles, G. Dif-Pradalier, C. Ehrlacher, D. Esteve, X. Garbet, P. Ghendrih, *et al.*, "A 5D gyrokinetic full-f global semi-Lagrangian code for flux-driven ion turbulence simulations," *Computer Physics Communications*, vol. 207, pp. 35–68, 2016.

[41] A. Brizard and T. Hahm, "Foundations of nonlinear gyrokinetic theory," *Reviews of modern physics*, vol. 79, no. 2, p. 421, 2007.

[42] P. Donnel, X. Garbet, Y. Sarazin, V. Grandgirard, Y. Asahi, N. Bouzat, E. Caschera, G. Dif-Pradalier, C. Ehrlacher, P. Ghendrih, *et al.*, "A multi-species collisional operator for full-f global gyrokinetics codes: Numerical aspects and verification with the gysela code," *Computer Physics Communications*, vol. 234, pp. 1–13, 2019.

[43] J. Abiteboul, X. Garbet, V. Grandgirard, S. Allfrey, P. Ghendrih, G. Latu, Y. Sarazin, and A. Strugarek, "Conservation equations and calculation of mean flows in gyrokinetics," *Physics of Plasmas*, vol. 18, no. 8, p. 082503, 2011.

[44] Y. Sarazin, V. Grandgirard, J. Abiteboul, S. Allfrey, X. Garbet, P. Ghendrih, G. Latu, A. Strugarek, G. Dif-Pradalier, P. Diamond, *et al.*, "Predictions on heat transport and plasma rotation from global gyrokinetic simulations," *Nuclear Fusion*, vol. 51, no. 10, p. 103023, 2011.

[45] Y. Sarazin, V. Grandgirard, P. Angelino, A. Casati, G. Dif-Pradalier, X. Garbet, P. Ghendrih, O. Gürcan, P. Hennequin, and R. Sabot, "Turbulence spectra and transport barriers in gyrokinetic simulations," in *AIP Conference Proceedings*, vol. 1069, pp. 325–330, American Institute of Physics, 2008.

[46] J. Rice, *Driven Rotation, Self-Generated Flow, and Momentum Transport in Tokamak Plasmas*, vol. 119. Springer Nature, 2022.

[47] J. Wilson, R. Bell, S. Bernabei, K. Hill, J. Hosea, B. LeBlanc, R. Majeski, R. Nazikian, M. Ono, C. Phillips, *et al.*, "Ion cyclotron range of frequencies heating and flow generation in deuterium-tritium plasmas," *Physics of Plasmas*, vol. 5, no. 5, pp. 1721–1726, 1998.

[48] Y. Lin, J. Rice, S. Wukitch, M. Greenwald, A. Hubbard, A. Ince-Cushman, L. Lin, M. Porkolab, M. Reinke, and N. Tsujii, "Observation of ion-cyclotron-frequency mode-conversion flow drive in tokamak plasmas," *Physical review letters*, vol. 101, no. 23, p. 235002, 2008.

[49] R. D. Hazeltine and J. D. Meiss, *Plasma confinement*. Courier Corporation, 2003.

[50] Y. Kim, P. Diamond, H. Biglari, and P. Terry, "Theory of resistivity-gradient-driven turbulence in a differentially rotating plasma," *Physics of Fluids B: Plasma Physics*, vol. 2, no. 9, pp. 2143–2150, 1990.

[51] B. D. Scott, P. Terry, and P. Diamond, "Saturation of Kelvin-Helmholtz fluctuations in a sheared magnetic field," *The Physics of fluids*, vol. 31, no. 6, pp. 1481–1491, 1988.

[52] N. Winsor, J. L. Johnson, and J. M. Dawson, "Geodesic acoustic waves in hydromagnetic systems," *The Physics of Fluids*, vol. 11, no. 11, pp. 2448–2450, 1968.

[53] K. Burrell, "Effects of ExB velocity shear and magnetic shear on turbulence and transport in magnetic confinement devices," tech. rep., General Atomic Co., 1996.

[54] J. Kim, W. Horton, D. Choi, S. Migliuolo, and B. Coppi, "Temperature anisotropy effect on the toroidal ion temperature gradient mode," *Physics of Fluids B: Plasma Physics*, vol. 4, no. 1, pp. 152–158, 1992.

[55] G. Dif-Pradalier, P. Diamond, V. Grandgirard, Y. Sarazin, J. Abiteboul, X. Garbet, P. Ghendrih, G. Latu, A. Strugarek, S. Ku, *et al.*, "Neoclassical physics in full distribution function gyrokinetics," *Physics of Plasmas*, vol. 18, no. 6, p. 062309, 2011.

[56] R. Waltz, J. Candy, and M. Rosenbluth, "Gyrokinetic turbulence simulation of profile shear stabilization and broken gyrobohm scaling," *Physics of Plasmas*, vol. 9, no. 5, pp. 1938–1946, 2002.

[57] P. Donnel, X. Garbet, Y. Sarazin, Y. Asahi, F. Wilczynski, E. Caschera, G. Dif-Pradalier, P. Ghendrih, and C. Gillot, "Turbulent generation of poloidal asymmetries of the electric potential in a tokamak," *Plasma Physics and Controlled Fusion*, vol. 61, no. 1, p. 014003, 2018.

[58] P. Ghendrih, G. Dif-Pradalier, C. Norscini, T. Cartier-Michaud, D. Estève, X. Garbet, V. Grandgirard, G. Latu, C. Passeron, and Y. Sarazin, "Self organisation of plasma turbulence: impact on radial correlation lengths," in *Journal of Physics: Conference Series*, vol. 561, p. 012008, IOP Publishing, 2014.

[59] P. Ghendrih, C. Norscini, T. Cartier-Michaud, G. Dif-Pradalier, J. Abiteboul, Y. Dong, X. Garbet, O. Gürcan, P. Hennequin, V. Grandgirard, *et al.*, "Phase space structures in gyrokinetic simulations of fusion plasma turbulence," *The European Physical Journal D*, vol. 68, no. 10, pp. 1–17, 2014.

[60] F. Jenko, W. Dorland, and G. Hammett, "Critical gradient formula for toroidal electron temperature gradient modes," *Physics of Plasmas*, vol. 8, no. 9, pp. 4096–4104, 2001.

[61] P. Helander, C. Beidler, T. Bird, M. Drevlak, Y. Feng, R. Hatzky, F. Jenko, R. Kleiber, J. Proll, Y. Turkin, *et al.*, "Stellarator and tokamak plasmas: a comparison," *Plasma Physics and Controlled Fusion*, vol. 54, no. 12, p. 124009, 2012.

[62] F. Merz and F. Jenko, "Nonlinear saturation of trapped electron modes via perpendicular particle diffusion," *Physical review letters*, vol. 100, no. 3, p. 035005, 2008.

[63] J. Lang, S. E. Parker, and Y. Chen, "Nonlinear saturation of collisionless trapped electron mode turbulence: Zonal flows and zonal density," *Physics of Plasmas*, vol. 15, no. 5, p. 055907, 2008.

[64] D. Ernst, J. Lang, W. Nevins, M. Hoffman, Y. Chen, W. Dorland, and S. Parker, "Role of zonal flows in trapped electron mode turbulence through nonlinear gyrokinetic particle and continuum simulation," *Physics of Plasmas*, vol. 16, no. 5, p. 055906, 2009.

[65] Y. Xiao and Z. Lin, "Turbulent transport of trapped-electron modes in collisionless plasmas," *Physical review letters*, vol. 103, no. 8, p. 085004, 2009.